

# Effect of Interfacial Octahedral Behavior in Ultrathin Manganite Films

E. J. Moon,<sup>\*,†</sup> P. V. Balachandran,<sup>†</sup> B. J. Kirby,<sup>‡</sup> D. J. Keavney,<sup>§</sup> R. J. Sichel-Tissot,<sup>†</sup> C. M. Schlepütz,<sup>§</sup> E. Karapetrova,<sup>§</sup> X. M. Cheng,<sup>||</sup> J. M. Rondinelli,<sup>†</sup> and S. J. May<sup>\*,†</sup>

<sup>†</sup>Department of Materials Science and Engineering, Drexel University, Philadelphia, Pennsylvania 19104, United States

<sup>‡</sup>Center for Neutron Research, National Institute of Standards and Technology, Gaithersburg, Maryland 20899, United States

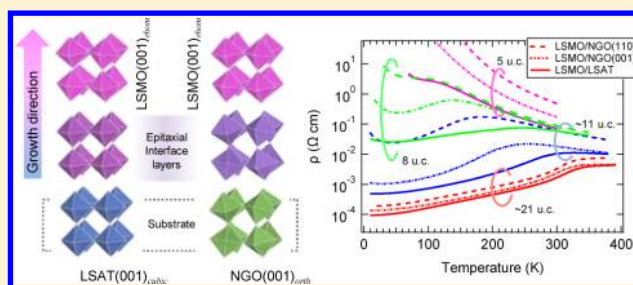
<sup>§</sup>X-ray Sciences Division, Advanced Photon Source, Argonne National Laboratory, Argonne, Illinois 60439, United States

<sup>||</sup>Department of Physics, Bryn Mawr College, Bryn Mawr, Pennsylvania 19010, United States

**S** Supporting Information

**ABSTRACT:** We investigate structural coupling of the  $\text{MnO}_6$  octahedra across a film/substrate interface and the resultant changes of the physical properties of ultrathin  $\text{La}_{2/3}\text{Sr}_{1/3}\text{MnO}_3$  (LSMO) films. In order to isolate the effect of interfacial  $\text{MnO}_6$  octahedral behavior from that of epitaxial strain, LSMO films are grown on substrates with different symmetry and similar lattice parameters. Ultrathin LSMO films show an increased magnetization and electrical conductivity on cubic ( $\text{LaAlO}_3$ )<sub>0.3</sub>( $\text{Sr}_2\text{AlTaO}_6$ )<sub>0.7</sub> (LSAT) compared to those grown on orthorhombic  $\text{NdGaO}_3$  (NGO) substrates, an effect that subsides as the thickness of the films is increased. This study demonstrates that interfacial structural coupling can play a critical role in the functional properties of oxide heterostructures.

**KEYWORDS:** Manganites, perovskites, epitaxial ultrathin film, interfacial properties



This study demonstrates that interfacial structural coupling can play a critical role in the functional properties of oxide heterostructures.

Epitaxial heterostructures of  $\text{ABO}_3$  perovskite oxides have attracted considerable interest owing to the possibility of coupling their rich variety of physical properties, such as ferromagnetism, superconductivity, and ferroelectricity, at abrupt interfaces between materials with different ground states.<sup>1,2</sup> One emerging route to stabilizing new behavior in perovskite heterostructures is through the control of  $\text{BO}_6$  octahedral rotations.<sup>3–5</sup> The topology of the corner shared  $\text{BO}_6$  octahedra is an established means to control phase stability between electronic and magnetic states, as has been demonstrated in numerous bulk systems where isovalent cation substitution is used to systematically alter octahedral rotations.<sup>6,7</sup> For instance, a reduction in electronic bandwidth driven by either reduced B–O–B bond angles ( $\theta$ ) or increased B–O bond lengths ( $d_{\text{B-O}}$ ) leads to a reduction in Curie temperatures in bulk ferromagnetic manganites.<sup>8</sup>

In thin film heterostructures, epitaxial strain and interfacial structural coupling offer additional means by which to control octahedral behavior allowing for the stabilization of local atomic structures distinct from the equilibrium bulk counterparts. While epitaxial strain coherently alters the octahedral behavior throughout an entire strained film,<sup>9–14</sup> recent work has demonstrated that interfacial coupling alters the amplitude of octahedral rotations over a much shorter length scale of 2–8 unit cells (uc).<sup>15–20</sup> However, a key obstacle impeding fully understanding and exploiting these local structural modifications is the difficulty in disentangling the distinct contributions of epitaxial strain and interfacial structural coupling and

establishing the penetration length of rotations across interfaces.

In this Letter, we isolate the influence of the substrate octahedral rotations on the electronic and magnetic properties of ultrathin  $\text{La}_{2/3}\text{Sr}_{1/3}\text{MnO}_3$  (LSMO) films. While the interfacial properties of LSMO heterostructures have received considerable interest,<sup>21–29</sup> the role played by octahedral behavior in controlling physical properties at LSMO-based interfaces remains largely unexplored. In bulk, LSMO exhibits the  $a^-a^-a^-$  tilt pattern<sup>30,31</sup> with uniform  $166.3^\circ$  B–O–B bond angles and a pseudocubic lattice parameter ( $a_{\text{pc}}$ ) of  $3.873 \text{ \AA}$ .<sup>8</sup> A systematic series of LSMO films were grown on cubic LSAT and orthorhombic NGO substrates. Both of these substrates have similar lattice parameters,  $\sim 3.868$  and  $\sim 3.862 \text{ \AA}$ , respectively, in the pseudocubic representation but differ in octahedral behavior allowing for interfacial octahedral coupling to be isolated as an independent variable. As shown in Figure 1a, LSAT lacks octahedral rotations ( $a^0a^0a^0$ ) and thus exhibits a uniform B–O–B bond angle of  $180^\circ$ . In contrast, NGO has large octahedral rotations ( $a^-a^-c^+$ ), leading to an average B–O–B bond angle of  $154^\circ$ .<sup>32</sup> Thus, films grown on LSAT would be expected to exhibit larger bond angles near the film/substrate interface compared to films grown on NGO, an effect that should manifest itself in bandwidth-related properties such

Received: January 20, 2014

Revised: March 27, 2014

Published: April 3, 2014

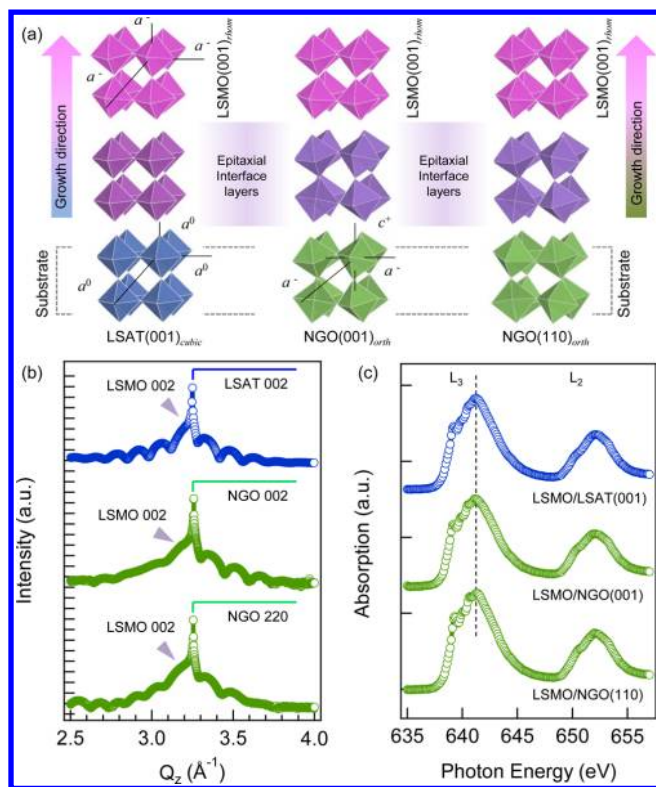


**Figure 1.** (a) Schematic of the LSMO/LSAT and LSMO/NGO heterostructures, highlighting the anticipated difference in  $\text{MnO}_6$  octahedral coupling across the substrate/film interface. The blue (green) color represents a LSAT (NGO) substrate. (b) XRD scans of  $\sim 11$  uc thick LSMO films grown on three different substrates, for example, LSAT(001), NGO(001), NGO(110). (c) XAS data of the Mn  $L_{2,3}$ -edge of LSMO films on the corresponding substrates measured at 130 K.

as conductivity and magnetization. The difference in rotation pattern also leads to a symmetry mismatch at the film/substrate interface. Using a multifaceted approach combining temperature dependent resistivity and magnetoresistivity (MR), X-ray magnetic circular dichroism (XMCD), polarized neutron reflectivity (PNR), and density functional theory calculations, we find increased magnetization and conductivity in ultrathin LSMO/LSAT compared to LSMO/NGO, demonstrating the prominent role played by near-interfacial atomic structure on the physical properties of correlated oxide films.

LSMO films were grown with oxide molecular beam epitaxy using an interrupted growth mode on LSAT(001) and NGO(001) and (110) substrates monitored by in situ reflection high energy electron diffraction (RHEED). To achieve smooth surfaces with single unit cell step heights for each substrate, NGO was annealed at 1075 °C for 8 h in  $\text{O}_2$  flowing, and LSAT was annealed at 1075 °C for 40 min under a  $\text{LaAlO}_3$  crystal in  $\text{O}_2$  flowing.<sup>33–35</sup> During deposition, the substrate temperature was held at  $\sim 600$  °C. An ozone/oxygen mixture ( $\sim 5/95\%$ ) was used as the oxidizing agent at a chamber pressure of  $\sim 1.1 \times 10^{-5}$  mbar. Film thickness and smooth surface morphology was confirmed by X-ray reflectivity (XRR) and atomic force microscopy (AFM). X-ray diffraction (XRD) was performed at the beamline 33-BM-C and resonant soft X-ray absorption spectroscopy (XAS) was performed in total electron yield mode at the beamline 4-ID-C of the Advanced Photon Source at Argonne National Laboratory.

PNR measurements were carried out on the Polarized Beam Reflectometer beamline at Center for Neutron Research, National Institute of Standards and Technology. Density functional theory (DFT) calculations were carried out within the spin-polarized generalized gradient approximation (GGA) plus Hubbard- $U$  method as implemented in the plane-wave pseudopotential code, Quantum ESPRESSO.<sup>36,37</sup> The Brillouin zone integrations were performed over a  $5 \times 5 \times 1$  Monkhorst–Pack k-point mesh centered at  $\Gamma$ .<sup>38</sup>

Figure 1a illustrates a hypothesized heterostructure of nonbulk symmetries in which the rotations of the  $\text{MnO}_6$  octahedra are modified in the LSMO (in pink) via interfacial coupling with the substrate (LSAT in blue and NGO in green). The two orientations of the NGO substrates differ in the direction of the out-of-phase (+) rotation axis and the in-plane bond lengths. In the (001) orientation, the + axis is along the growth direction and the in-plane distance between neighboring Ga atoms is 3.863 Å along both orthogonal directions. In the (110) orientation, an in-phase (–) rotation axis is along the growth direction and the in-plane distances between Ga atoms are 3.863 and 3.854 Å.<sup>32</sup> Thus, the LSMO films on NGO (110) are under slightly higher average compressive stress than those on NGO (001). Synchrotron-based XRD was performed to determine the basic structural properties of the films. Figure 1b shows the diffraction around the pseudocubic (0 0 2) reflection of the  $\sim 11$  unit cell (uc) thick LSMO films grown on LSAT(001), NGO(001), and NGO(110), respectively, as a function of the out-of-plane momentum transfer vector,  $Q_z$ . The LSMO films show the expected Bragg reflection for  $c$ -axis oriented layers and clear Kiessig fringes testifying to the quality of the film. Importantly, the  $Q_z$  value of the (0 0 2) peak is very similar for all samples, confirming that the films have the same  $c$ -axis lattice parameters. Furthermore, XAS Mn  $L_{2,3}$ -edge results confirm that the nominal mixed valence state of  $\text{Mn}^{3+}/\text{Mn}^{4+}$  is the same in all films of the same thickness (Figure 1c). While there are changes to the Mn XAS spectra as the film thickness is reduced (see Supporting Information) consistent with previous work on LSMO films,<sup>39</sup> the Mn spectra are not altered by the different substrates. These results serve as evidence that differences in composition and/or strain are not driving the observed deviations in physical properties discussed below.

The surface morphology and thicknesses of the films were characterized using multiple techniques to confirm the viability of comparing films of the same nominal thickness. Figure 2a shows a reflective high energy electron diffraction (RHEED) image of a 12 uc thick film on a NGO(001) substrate; the pattern is typical of a perovskite surface. Atomic force microscopy reveals the films have smooth morphologies (Figure 2b,c). In order to verify the thicknesses of the films, X-ray reflectivity was measured and fit using the GenX software. Film thickness was determined based on the distance from the film/substrate interface at which the scattering length density equals half that of the film's value. As shown in Figure 2d, the obtained thicknesses for the  $\sim 11$  uc thick films are 4.15 nm (10.7 uc), 4.67 nm (12.0 uc), and 4.38 nm (11.3 uc) for the films grown on LSAT (001), NGO (001), and NGO (110), respectively. On the basis of the reflectivity analysis, we estimate the difference in the film-to-film thickness to be 10% or less, confirming that comparisons between films of nominally equal thickness are accurate to a unit cell or less.

DC transport measurements were performed to elucidate the electronic and magnetic properties of the films. Figure 3a shows

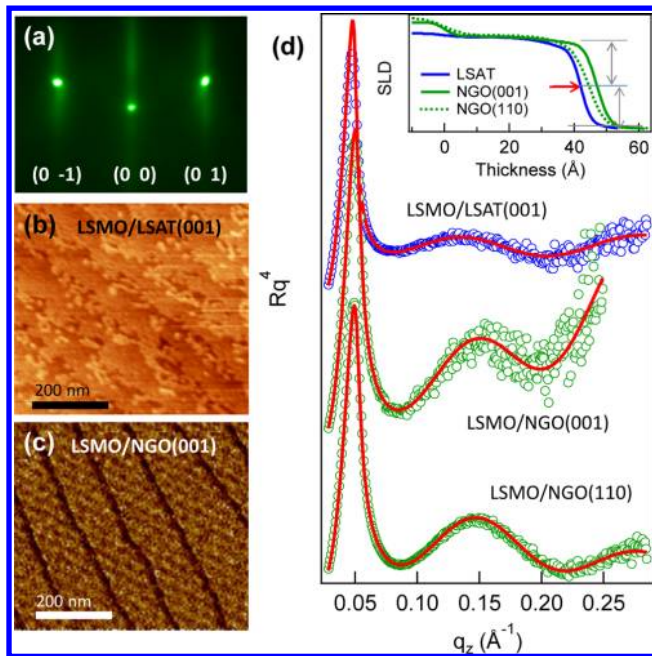


**Figure 2.** (a) RHEED image of the 12 uc LSMO ultrathin film on NGO(001) after growth. Atomic force microscopy shows the smooth film morphology. The 11 uc thick film on LSAT substrate is shown in (b); the 22 uc thick film on NGO(001) is shown in (c). (d) X-ray reflectivity data (open symbols) and fits (solid lines) for the  $\sim 11$  uc films. The film thicknesses are obtained from the half-maximum of the normalized scattering length density (inset).

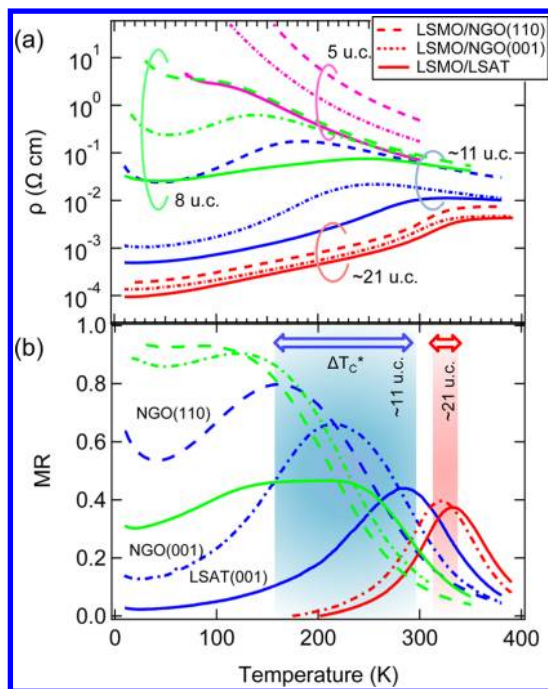


**Figure 3.** (a) Resistivity ( $\rho$ ) as a function of temperature in zero field for ultrathin LSMO films of varying thickness (5, 8,  $\sim 11$ , and  $\sim 21$  uc) grown on symmetry-mismatched substrates (NGO and LSAT). (b) The corresponding MR ( $(\rho_0 - \rho_{H=7T})/\rho_0$ ). The enclosed boxes highlight the variation of  $MR_{\max}$  for  $\sim 21$  and  $\sim 11$  uc and  $\Delta T_{C^*}$  is the range of  $MR_{\max}$  temperatures.

resistivity versus temperature for the LSMO films. A systematic trend is observed in which the films grown on LSAT exhibit the

lowest resistivity values and the highest temperature for the local resistivity maximum, which in the manganites is typically associated with a ferro-to-paramagnetic transition. For instance in the  $\sim 11$  uc films, the resistivity maximum occurs at  $\sim 310$  and  $\sim 170$  K in films on LSAT and NGO (110), respectively, while the low-temperature resistivity differs by almost 2 orders of magnitude. Similarly, the 5 and 8 uc films on LSAT exhibit a lower resistivity compared to those on NGO. Local resistivity maxima are observed in the 8 uc films, while the 5 uc films are insulating over the measured temperature range. The behavior on LSAT compared to NGO is consistent with a scenario where the LSMO on LSAT exhibits reduced octahedral rotations near the interface due to the cubic nature of the LSAT substrate, whereas the rotations are enhanced in the films grown on NGO. The larger rotations in the films grown on NGO would be expected to reduce the electronic bandwidth near the interface leading to a suppression of electrical conductivity, as observed. The deviation between the films grown on LSAT and NGO is enhanced as the film thickness is reduced, consistent with a transition from bulk-dominated to interface-dominated behavior. In the case of  $\sim 21$  uc LSMO, the temperature-dependent resistivity shows a similar trend for all three films indicating that bulklike behavior is dominant at that thickness. This result is consistent with previous studies of strained 22 nm thick LSMO films on LSAT and NGO (110), which were found to exhibit nearly identical electronic and magnetic properties.<sup>40</sup>

As shown in Figure 3b, similar trends are observed in the MR, which often exhibits a maximum at the magnetic ordering temperature of manganites. Here, we define  $MR = (\rho_0 - \rho_{(H=7T)})/\rho_0$ , where  $\rho_0$  is the zero-field resistivity. A suppression in the temperature at which the MR is maximized ( $T_{C^*}$ ) is observed in the 8 and  $\sim 11$  uc films grown on NGO compared to LSAT, whereas the MR difference in the  $\sim 21$  uc films is minimal. In both the resistivity and MR measurements, the films grown on NGO (001) exhibit behavior consistent with larger bandwidth compared to the films on NGO (110). We attribute this to the slightly larger compressive strain induced by the NGO (110) substrate compared to the NGO (001) substrate. Additionally, the difference in the orientations of the out-of-phase rotation axis may be contributing to differences in the physical properties.

In order to determine the magnetic depth profile across interface between substrate/film, we performed PNR on 18 uc LSMO films on LSAT, NGO (001), and NGO (110) substrates, as shown in Figure 4 (a–c), respectively. The films were field-cooled to 100 K and measured with a 0.5 T field in-the-plane of the films. Data fitting was performed using both the *co\_refine*<sup>41</sup> and NIST Refl1D<sup>42</sup> software routines, the results from which were in good agreement. Fits to the data reveal a reduced magnetization in all three samples at the substrate/film interface that extends over  $\sim 5$  uc (Figure 4d). Models without the reduced interfacial magnetization could not accurately reproduce the measured PNR data (see Supporting Information). The reduced interfacial magnetization does not coincide with a change in the nuclear scattering length density profile, indicating that the change in magnetization near the interface is not arising from a local compositional variation. However, we note that the exact width of the interfacial region of reduced magnetization could not be uniquely determined based on fitting the PNR data. Consistent with the trend in the resistivity data, the film on LSAT has the largest magnetization, followed by the films on NGO. The magnetic profiles also

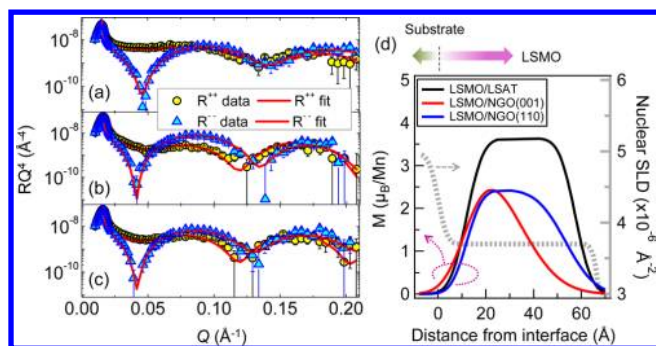


**Figure 4.** Measured (open symbols) and fit (solid lines) PNR data of (a) LSMO/LSAT, (b) LSMO/NGO(001), and (c) LSMO/NGO(110). (d) The magnetic depth profile (solid lines) reveals a reduced interfacial magnetization that extends over  $\sim 5$  uc, while the nuclear scattering length density (dotted line), shown here for LSMO/LSAT, is constant over the region of reduced magnetization.

reveal the presence of a reduced magnetization at the film/air interface.<sup>43</sup> Unexpectedly, we find that the LSMO/NGO (001) exhibits a larger suppression of magnetization at the surface than the other two samples. While the origin of this behavior is unknown, we note that the XAS of this particular sample suggests increased surface oxidation compared to the 18 uc LSMO/LSAT and LSMO/NGO (110), as shown in the Supporting Information. However, the XAS of the 5, 11, and 21 uc films do not exhibit differences for films of the same thickness. Therefore, we believe the surface behavior of 18 uc LSMO/NGO (001) is an outlier and not responsible for the physical behavior observed in the other samples.

Next, we turn our attention to magnetic measurements performed with XMCD, in which the differences in the absorption of right and left circularly polarized X-rays were measured at the Mn L edge. Figure 5a shows the Mn 2p ( $\rightarrow 3d$ ) XMCD spectra of the films grown on the three substrates measured at 130 K under 0.5 T. The line shapes of the spectra are comparable to previously published data for this LSMO composition.<sup>43</sup> Furthermore, the spectra show that the  $L_{2,3}$ -edge peak position is independent of the substrate confirming the constant nominal valence of all samples (see also Figure 1c). Consistent with the transport data, the dichroism signal of  $\sim 11$  and 5 uc LSMO is considerably reduced in the films on NGO while the XMCD magnitude from the  $\sim 21$  uc LSMO films are similar. The XMCD intensity of the films on NGO (001) is also larger than those on NGO (110), also similar to the behavior observed in the transport data.

Figure 5b displays the temperature at which the MR is maximized ( $T^*$ ) and XMCD peak intensity of the Mn  $L_3$  peak ( $I_{\text{XMCD}}$ ) as a function the film thickness. For  $d > 12$  uc, all three films exhibit bulklike properties, as the interfacial contribution to the total film volume becomes small. Thus, in this regime the octahedral behavior for the majority of the film is determined by epitaxial strain and the lattice parameters imposed by the substrate, which are very similar for LSAT and NGO. In contrast, for the thinner films the magnetic signatures exhibit a systematic suppression in LSMO/NGO compared to LSMO/LSAT. This indicates that in this thickness regime the film octahedral behavior, and therefore properties dependent on electronic bandwidth, is strongly dependent on the substrate octahedral behavior.

To better understand the local Mn–O–Mn distortions near the substrate/film interface, we have carried out DFT

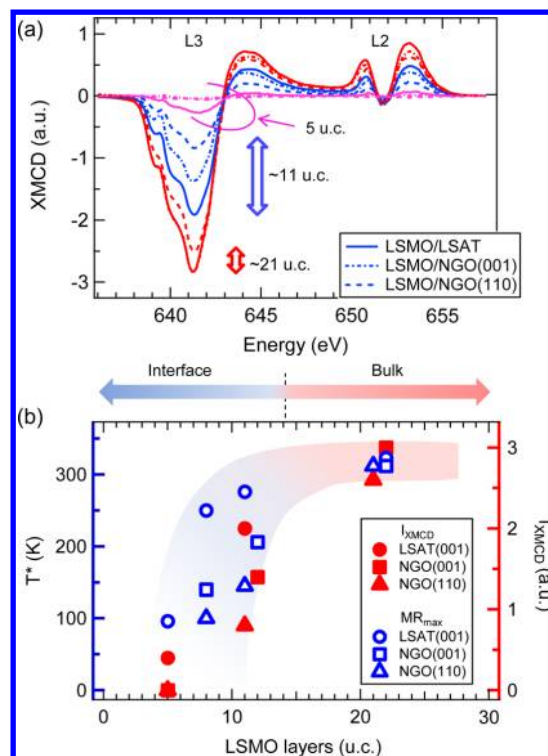


**Figure 5.** (a) Mn  $L_2$  and  $L_3$  edge XMCD curves of LSMO films of various thickness measured at 130 K under 0.5 T. (b)  $T^*$  ( $\text{MR}_{\text{max}}$  peak position, open symbol in blue) and intensity of the Mn  $2p_{3/2}$  multiplet ( $I_{\text{XMCD}}$ , solid symbol in red) as a function of LSMO film thickness.

calculations. Note that our objective is to study the trend in the Mn- $e_g$  orbital bandwidth and Mn–O–Mn bond distortions near the interface, when the substrate either lacks octahedral rotations or has large octahedral rotations. Therefore, we constructed two supercells, each containing 60 and 100 atoms, to simulate the structures of LSMO grown on (001) planes of a gallate substrate with cubic ( $a^0a^0a^0$ ; no octahedral rotations) and orthorhombic ( $a^-a^-c^+$ ) symmetries, respectively. We do not consider free surfaces in our calculations. To eliminate additional degrees of freedom and changes in chemistry across the substrate–film interface, we select LaGaO<sub>3</sub> as our substrate constrained to have the lattice constants and atomic coordinates of the orthorhombic NdGaO<sub>3</sub> and cubic LSAT structures. Here, we constrained the in-plane lattice constants of LSMO to match that of the hypothetical substrates and then fully relaxed the atomic coordinates and out-of-plane lattice constants starting from the bulk LSMO tilt pattern.<sup>44</sup> The top panels of Figure 6 show the ground state crystal structures of coherent LSMO with the first few layers (in purple) on a cubic (panel a in blue) and an orthorhombic substrate (panel b in green). The middle panels display the B–O–B bond angles along the out-of-plane (red squares) and in-plane (black circles) directions. The LSMO on the cubic substrate (in panel a) shows straighter out-of-plane bond angles (closer to 180°) relative to the calculated bulk value (165.6°, orange line), whereas its in-plane bond angles are suppressed near the interface. The LSMO on the orthorhombic substrate, as shown in (panel b), exhibits more distorted in- and out-of-plane rotations in the vicinity of the interface compared to their bulk values.

The effect of interfacial coupling (between layers 1 and 2 in the middle panels) and changes in rotation amplitudes is also

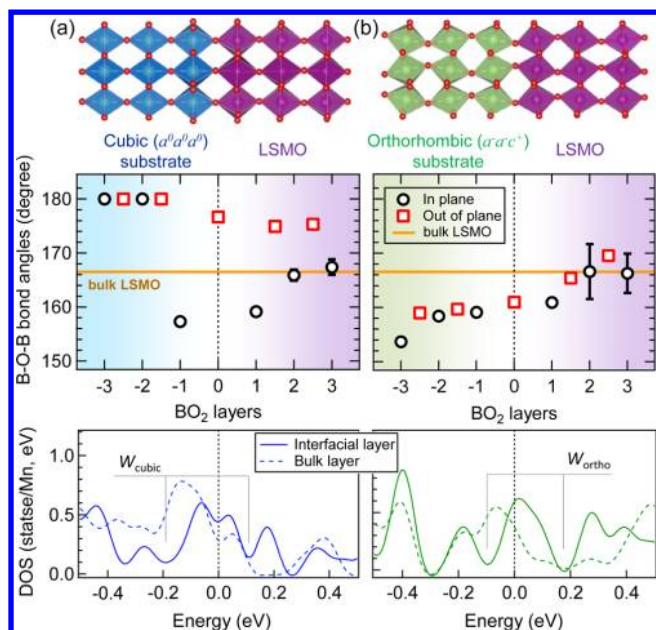


**Figure 6.** Density functional calculations of the B–O–B bond angles resolved along the film normal (red squares) and in-plane (black circles). For comparison, the bond angle of bulk LSMO is shown by a solid line located at  $166.3^\circ$ . The mean values of the Mn–O–Mn bond angles and their standard deviations are shown as error bars. Error bars smaller than the size of the data point are not visible. PDOS spectra of majority spin Mn  $e_g$  orbitals (bottom panels) for the first  $\text{MnO}_2$  layer from the interface centered at  $E_F$ , showing a narrowing of the  $e_g$  orbital bandwidth for LSMO on an orthorhombic substrate (right) compared to LSMO on a cubic substrate (left). For the bulk layers, we have averaged the noninterfacial PDOS.

evident in the Mn 3d projected density of states (PDOS) spectra. The bottom panels of Figure 6 show the PDOS spectra for the first three  $\text{MnO}_2$  layers from the interface centered at the Fermi level ( $E_F$ ). The  $e_g$  orbital bandwidths at  $E_F$  for the interfacial- $\text{MnO}_2$  layers are found to be relatively narrower for LSMO on orthorhombic (right) compared to LSMO on cubic substrate (left). Since the  $e_g$  orbital bandwidth directly impacts the transport properties,<sup>45,46</sup> we infer from our DFT calculations that the experimentally reduced electrical conductivity (see Figure 3 (a)) for LSMO on NGO (001) is due to its relatively more buckled Mn–O bond network. In addition, we note that the deviation would be more pronounced as the film thickness is reduced, because the volume of material that is more distorted increases. This behavior is consistent with a transition from bulk-dominated to interface/surface-dominated behavior.

The bonding parameters obtained from DFT also enable an approximate comparison to bulk  $A_{0.7}A'_{0.3}\text{MnO}_3$  manganites, for which the relationship between structure, electronic bandwidth ( $W$ ), and the Curie temperature ( $T_C$ ) has been studied in detail.<sup>8</sup> Radaelli and coauthors used the expression  $W \propto \cos \omega / d^{3.5}$ , where  $\omega$  is given by  $(\pi - \theta)/2$ , to correlate  $T_C$  with structural driven changes in  $W$  in bulk manganites. They showed that  $\sim 1$ – $2\%$  decreases in  $W$  resulted in 100–150 K reductions in  $T_C$ . Applying the same equation to our structural data and averaging over the 6 values of  $d_{\text{B-O}}$  and  $\omega$  in a  $\text{MnO}_6$  octahedra, we find a  $\sim 0.8\%$  reduction in  $W$  in the interfacial most LSMO layer on the orthorhombic substrate compared to the cubic substrate. Therefore, the large changes in  $T_C$  that we observed due to subtle changes in the LSMO atomic structure

are consistent with behavior in bulk manganites, albeit achieved here without chemical pressure using only substrate-induced modifications to the rotation network. Finally, we note that the change in  $W$  as calculated from the bonding parameters is significantly less than the difference in width of the Mn  $e_g$  band at  $E_F$  calculated by DFT, which is  $\sim 9\%$  (shown in the bottom panels of Figure 6). This suggests that the equation for  $W$  given above likely underestimates the sensitivity of electronic structure to modifications or distortions of the atomic structure.

In conclusion, we have shown significant deviations in the electronic and magnetic properties of ultrathin LSMO films grown on cubic and orthorhombic substrates, despite the same strain state imposed by these substrates. The origin of this effect is attributed to interfacial structural coupling, leading to reduced  $\text{MnO}_6$  rotations near the film/substrate interface in the LSMO/LSAT compared to LSMO/NGO. This study demonstrates that modifications to  $\text{BO}_6$  rotations at heterointerfaces can play a critical role in the functional properties of oxide heterostructures.

## ■ ASSOCIATED CONTENT

### Supporting Information

Additional information regarding XAS and the PNR fitting. This material is available free of charge via the Internet at <http://pubs.acs.org>.

## ■ AUTHOR INFORMATION

### Corresponding Authors

\*E-mail: (E.J.M.) [em582@drexel.edu](mailto:em582@drexel.edu).

\*E-mail: (S.J.M.) [smay@coe.drexel.edu](mailto:smay@coe.drexel.edu).

### Notes

The authors declare no competing financial interest.

## ■ ACKNOWLEDGMENTS

We thank Leszek Wielunski for RBS measurements and Goran Karapetrov for access to his AFM instrument. E.J.M. and S.J.M. were supported by the U.S. Army Research Office under Grant W911NF-12-1-0132. Acquisition of the PPMS was supported by the U.S. Army Research Office under Grant W911NF-11-1-0283. P.V.B. and J.M.R. were supported by DARPA and ARO under Grant N66001-12-4224 and W911NF-12-1-0133, respectively. DFT calculations were carried out at the high-performance computing cluster (CARBON) of the Center for Nanoscale Materials (Argonne National Laboratory) supported by the US DOE (DE-AC02-06CH11357). Use of the Advanced Photon Source, an Office of Science User Facility operated for the U.S. Department of Energy (DOE) Office of Science by Argonne National Laboratory, was supported by the U.S. DOE under Contract No. DE-AC02-06CH11357. X.M.C. was supported by NSF DMR-1053854.

## ■ REFERENCES

- (1) Hwang, H. Y.; Iwasa, Y.; Kawasaki, M.; Keimer, B.; Nagaosa, N.; Tokura, Y. *Nat. Mater.* **2012**, *11*, 103.
- (2) Zubko, P.; Gariglio, S.; Gabay, M.; Ghosez, P.; Triscone, J.-M. *Annu. Rev. Condens. Matter Phys.* **2011**, *2*, 141.
- (3) Bousquet, E.; Dawber, M.; Stucki, N.; Lichtensteiger, C.; Hermet, P.; Gariglio, S.; Triscone, J. M.; Ghosez, P. *Nature* **2008**, *452*, 732.
- (4) Rondinelli, J. M.; May, S. J.; Freeland, J. W. *MRS Bull.* **2012**, *37*, 261.
- (5) Benedek, N. A.; Mulder, A. T.; Fennie, C. J. *J. Solid State Chem.* **2012**, *195*, 11.
- (6) Medarde, M. L. *J. Phys.: Cond. Matter* **1997**, *9*, 1679.

- (7) Chmaissem, O.; Dabrowski, B.; Kolesnik, S.; Mais, J.; Brown, D. E.; Kruk, R.; Prior, P.; Pyles, B.; Jorgensen, J. D. *Phys. Rev. B* **2001**, *64*, 134412.
- (8) Radaelli, P. G.; Iannone, G.; Marezio, M.; Hwang, H. Y.; Cheong, S.-W.; Jorgensen, J. D.; Argyriou, D. N. *Phys. Rev. B* **1997**, *56*, 8265.
- (9) Wakabayashi, Y.; Sawa, H.; Nakamura, M.; Izumi, M.; Miyano, K. *Phys. Rev. B* **2004**, *69*, 144414.
- (10) Xie, C. K.; Budnick, J. I.; Hines, W. A.; Wells, B. O.; Woicik, J. C. *Appl. Phys. Lett.* **2008**, *93*, 182507.
- (11) May, S. J.; Kim, J.-W.; Rondinelli, J. M.; Karapetrova, E.; Spaldin, N. A.; Bhattacharya, A.; Ryan, P. J. *Phys. Rev. B* **2010**, *82*, 014110.
- (12) Vailionis, A.; Boschker, H.; Siemons, W.; Houwman, E. P.; Blank, D. H. A.; Rijnders, G.; Koster, G. *Phys. Rev. B* **2011**, *83*, 064101.
- (13) Hwang, J.; Zhang, J. Y.; Son, J.; Stemmer, S. *Appl. Phys. Lett.* **2012**, *100*, 191909.
- (14) Rotella, H.; Luders, U.; Janolin, P.-E.; Dao, V. H.; Chateigner, D.; Feyherherm, R.; Dudzik, E.; Prellier, W. *Phys. Rev. B* **2012**, *85*, 184101.
- (15) Jia, C. L.; Mi, S. B.; Faley, M.; Poppe, U.; Schubert, J.; Urban, K. *Phys. Rev. B* **2009**, *79*, 081405.
- (16) Borisevich, A. Y.; Chang, H. J.; Huijben, M.; Oxley, M. P.; Okamoto, S.; Niranjana, M. K.; Burton, J. D.; Tsymbal, E. Y.; Chu, Y. H.; Yu, P.; et al. *Phys. Rev. Lett.* **2010**, *105*, 087204.
- (17) Rondinelli, J. M.; Spaldin, N. A. *Phys. Rev. B* **2010**, *82*, 113402.
- (18) He, J.; Borisevich, A.; Kalinin, S. V.; Pennycook, S. J.; Pantelides, S. T. *Phys. Rev. Lett.* **2010**, *105*, 227203.
- (19) May, S. J.; Smith, C. R.; Kim, J.-W.; Karapetrova, E.; Bhattacharya, A.; Ryan, P. J. *Phys. Rev. B* **2011**, *83*, 153411.
- (20) Hwang, J.; Son, J.; Zhang, J. Y.; Janotti, A.; Van de Walle, C. G.; Stemmer, S. *Phys. Rev. B* **2013**, *87*, 060101.
- (21) Yamada, H.; Ogawa, Y.; Ishii, Y.; Sato, H.; Kawasaki, M.; Akoh, H.; Tokura, Y. *Science* **2004**, *305*, 646–648.
- (22) Kavich, J. J.; Marusawithana, M. P.; Freeland, J. W.; Ryan, P.; Zhai, X.; Kodama, R. H.; Eckstein, J. N. *Phys. Rev. B* **2007**, *76*, 014410.
- (23) Huijben, M.; Martin, L. W.; Chu, Y.-H.; Holcomb, M. B.; Yu, P.; Rijnders, G.; Blank, D. H. A.; Ramesh, R. *Phys. Rev. B* **2008**, *78*, 094413.
- (24) Kourkoutis, L.; Song, J. H.; Hwang, H. Y.; Muller, D. A. *Proc. Natl. Acad. Sci. U.S.A.* **2010**, *107*, 11682–11685.
- (25) Bruno, F. Y.; Garcia-Barriocanal, J.; Varela, M.; Nemes, N. M.; Thakur, P.; Cezar, J. C.; Brookes, N. B.; Rivera-Calzada, A.; Garcia-Hernandez, M.; Leon, C.; Okamoto, S.; Pennycook, S. J.; Santamaria, J. *Phys. Rev. Lett.* **2011**, *106*, 147205.
- (26) Boschker, H.; Verbeeck, J.; Egoavil, R.; Bals, S.; van Tendeloo, G.; Huijben, M.; Houwman, E. P.; Koster, G.; Blank, D. H. A.; Rijnders, G. *Adv. Funct. Mater.* **2012**, *22*, 2235–2240.
- (27) Lee, J.-S.; Arena, D. A.; Santos, T. S.; Nelson, C. S.; Nyun, S. I.; Shim, J. H.; Kao, C.-C. *Phys. Rev. B* **2012**, *85*, 235125.
- (28) Ziese, M.; Bern, F.; Pippel, E.; Hesse, D.; Vrejoiu, I. *Nano Lett.* **2012**, *12*, 4726–4281.
- (29) Petrov, A. Yu.; Torrelles, X.; Verna, A.; Xu, H.; Cossaro, A.; Pedio, M.; Garcia-Barriocanal, J.; Castro, G. R.; Davison, B. A. *Adv. Mater.* **2013**, *25*, 4043–4048.
- (30) Glazer, A. M. *Acta Cryst. B* **1972**, *28*, 3384.
- (31) Woodward, P. M. *Acta Cryst. B* **1997**, *53*, 32.
- (32) Vasylychko, L.; Akselrud, L.; Morgenroth, W.; Bismayer, U.; Matkovskii, A.; Savvitskii, D. *J. Alloys Comp.* **2000**, *297*, 46.
- (33) Ohnishi, T.; Takahashi, K.; Nakamura, M.; Kawasaki, M.; Yoshimoto, M.; Koinuma, H. *Appl. Phys. Lett.* **1999**, *74*, 2531.
- (34) Dirsyte, R.; Schwarzkopf, J.; Wagner, G.; Lienemann, J.; Busch, M.; Winter, H.; Fornari, R. *Appl. Sur. Sci.* **2009**, *255*, 8685.
- (35) Ngai, J. H.; Schwendemann, T. C.; Walker, A. E.; Segal, Y.; Walker, F. J.; Altman, E. I.; Ahn, C. H. *Adv. Mater.* **2010**, *22*, 2945.
- (36) Giannozzi, P.; Baroni, S.; Baroni, N.; Calandra, M.; Car, R.; Cavazzoni, C.; Ceresoli, D.; Chiarotti, G. L.; Cococcioni, M.; Dabo, I.; Dal Corso, A.; de Gironcoli, S.; Fabris, S.; Fratesi, G.; Gebauer, R.; Gerstmann, U.; Gougoussis, C.; Kokalj, A.; Lazzeri, M.; Martin-Samos, L.; Marzari, N.; Mauri, F.; Mazzarello, R.; Paolini, S.; Pasquarello, A.; Paulatto, L.; Sbraccia, C.; Scandolo, S.; Sclauzero, G.; Seitsonen, A. P.; Smogunov, A.; Umari, P.; Wentzcovitch, R. M. *J. Phys.: Condens. Matter* **2009**, *21*, 395502.
- (37) We used an effective Hubbard term<sup>47</sup> of  $2\text{ eV}^{48}$  to treat the correlated Mn-3d electrons with ferromagnetic spin order imposed. The core and valence electrons were treated with ultrasoft pseudopotentials<sup>49</sup> and PBEsol exchange-correlation functional.<sup>50,51</sup>
- (38) Monkhorst, H. J.; Pack, J. D. *Phys. Rev. B* **1976**, *13*, 5188.
- (39) Chopdekar, R. V.; Arenholz, E.; Suzuki, Y. *Phys. Rev. B* **2009**, *79*, 104417.
- (40) Adamo, C.; Ke, X.; Wang, H. Q.; Xin, H. L.; Heeg, T.; Hawley, M. E.; Zander, W.; Schubert, J.; Schiffer, P.; Muller, D. A.; et al. *Appl. Phys. Lett.* **2009**, *95*, 112504.
- (41) Fitzsimmons, M. R.; Majkrzak, C. F. In *Modern Techniques for Characterizing Magnetic Materials*; Zhu, Y., ed.; Springer: New York, 2005; Chapter 3, pp 107–155.
- (42) Kirby, B. J.; Kienzle, P. A.; Maranville, B. B.; Berk, N. F.; Krycka, J.; Heinrich, F.; Majkrzak, C. F. *Curr. Opin. Colloid Interface Sci.* **2012**, *17*, 44.
- (43) Park, J.-H.; Vescovo, E.; Kim, H.-J.; Kwon, C.; Ramesh, R.; Venkatesan, T. *Phys. Rev. Lett.* **1998**, *81*, 1953.
- (44) We constrained atoms in the second layer for the cubic substrate and the bottom layer for the orthorhombic substrate to remain static, so as to maintain the bulk distortions. In both cases, LSMO exhibits the  $a^-a^-c^-$  pattern.
- (45) Pickett, W. E.; Singh, D. J. *Phys. Rev. B* **1996**, *53*, 1146.
- (46) Sacchetti, A.; Guidi, M. C.; Arcangeletti, E.; Nucara, A.; Calvani, P.; Piccinini, M.; Marcelli, A.; Postorino, P. *Phys. Rev. Lett.* **2006**, *96*, 035503.
- (47) Dudarev, S. L.; Botton, G. A.; Savrasov, S. Y.; Humphreys, C. J.; Sutton, A. P. *Phys. Rev. B* **1998**, *57*, 1505.
- (48) Ma, C.; Yang, Z.; Picozzi, S. *J. Phys.: Condens. Matter* **2006**, *18*, 7717.
- (49) Vanderbilt, D. *Phys. Rev. B* **1990**, *41*, 7892.
- (50) Perdew, J. P.; Burke, K.; Ernzerhof, M. *Phys. Rev. Lett.* **1996**, *77*, 3865.
- (51) Perdew, J. P.; Ruzsinszky, A.; Csonka, G. I.; Vydrov, O. A.; Scuseria, G. E.; Constantin, L. A.; Zhou, X.; Burke, K. *Phys. Rev. Lett.* **2008**, *100*, 136406.